Vol. 48, No. 3 (2026) 632-644, DOI: 10.24874/ti.2098.12.25.04

Tribology in Industry

www.tribology.rs

RESEARCH

Mathematical Modeling of Surface Roughness Effects in Shaft-Hub Interference Fits

Manuel Salgado-Cruz[a,b,c], Claudia Cortés-García[a,*], Eladio Martínez-Rayón[a], Jorge Colín-Ocampo[a], Luis Vázquez-Sánchez[a], José M. A. Castillo-Minjarez[b], Javier Cortés-Benigno[c], Gibran J. Garnica-Castro[c], Oliver M. Huerta-Chávez[d]

[a]*CENIDET, National Technologic of Mexico, Mechanic Engineering Department, Apatzingán 212, Cuernavaca, Mor. 62490, Mexico,*
[b]*Technological University of Tecámac, Industrial Electromechanical Department, Mexico-Pachuca Federal Highway, KM 37.5, Tecámac, Edo. Mex. 55740, Mexico,*
[c]*National Autonomous University of Mexico, High Technology Unit, C.U., Coyoacán, CDMX 03000, Mexico,*
[d]*National Polytechnic Institute, Sepi Esime Ticomán, Gustavo A. Madero, CDMX 07340, Mexico.*

Keywords:

Shaft–hub interference fit
Mathematical modeling
Turning process
Surface roughness
Extraction force

* Corresponding author:

Claudia Cortés García
E-mail: claudia.cg@cenidet.tecnm.mx

Received: 3 December 2025
Revised: 3 February 2026
Accepted: 14 April 2026

ABSTRACT

This study presents an analytical model to evaluate the impact of turning-induced surface roughness on the mechanical response of shaft-hub interference fits. Surface topography is modeled using a sinusoidal function linked to machining parameters, enabling the prediction of real contact area, contact pressure, and extraction force. Analyzing three profile conditions, results show that peak-dominated surfaces significantly reduce joint strength, while valley-dominated profiles drastically increase extraction capacity due to mechanical interlocking. Validated against experimental data, this model offers a fast and reliable alternative to Finite Element Analysis (FEA) for designing interference fits under realistic surface conditions.

CC BY NC

© 2026 Published by Faculty of Engineering

1. INTRODUCTION

Shaft-hub interference fits are fundamental components in mechanical power transmission, widely used in industries ranging from automotive to aerospace due to their ability to transmit torque through friction without the need for additional fasteners. Traditionally, the design of these joints has relied on the analytical solutions provided by Lamé's equations for thick-walled cylinders, often assuming perfectly smooth contact surfaces. However, modern engineering demands a more precise understanding of the interface, as classical theories frequently neglect the significant influence of micro-topography on the joint's mechanical integrity.

The complexity of contact between rough surfaces is a cornerstone of modern tribology. Modern secondary sources, such as those by Barber [1] and Johnson [2], have superseded classical primary models by providing a more comprehensive framework for understanding how real contact area often only a fraction of the nominal area dictates pressure distribution. Williams [3] further emphasizes that surface finish is not merely a geometric attribute but a critical factor in frictional performance. Recent studies have expanded these concepts; for instance, Izard et al. [4] utilized Finite Element Analysis (FEA) to demonstrate that the friction coefficient and stress distributions are highly sensitive to surface finish variations. Similarly, Au-Yeung et al. [5] highlighted the importance of surface conditions in the non-destructive disassembly and sustainable remanufacturing of interference fits.

The mechanical strength of these joints is deeply rooted in the manufacturing process. Previous research by Salgado-Cruz et al. [6,7] has shown through experimental and numerical methods that the setting and extraction efforts are directly tied to the roughness generated during CNC turning. This is supported by Yang and Tarng [8], who investigated how turning parameters specifically alter surface integrity and roughness profiles. Furthermore, the evolution of the static friction coefficient under varying initial contact pressures remains a key variable in predicting joint failure [9].

In addition to geometry, advanced physical phenomena such as elasto-plasticity and thermal effects play a vital role. Abdo et al. [10] recently conducted elasto-plastic contact analyses showing that asperity deformation often exceeds the elastic limit, a factor that influences the overall interference. Thermomechanical effects may also influence the performance of interference fits, particularly under elevated-temperature operation, where thermal expansion and temperature-dependent material behavior can modify the interference and contact pressure [11].

Modern multiscale modeling approaches [12] and studies on micro-scale roughness [13] have paved the way for more sophisticated analytical tools. One of the most critical phenomena identified in high-roughness fits is the mechanical "interlocking" effect, where micro-topographical indentations create a physical barrier against sliding, significantly raising the extraction capacity [14]. Additionally, emerging research suggests that thin-film coatings may further optimize these connections by modifying the joining process [15].

This paper proposes a mathematical model based on a sinusoidal representation of surface roughness to evaluate its effect on the mechanical response of shaft-hub fits. By categorizing the roughness distribution into three distinct cases (Peaks, Mean line, and Valleys), this study provides a robust analytical framework to predict the real contact area and effective extraction force, incorporating the complex interactions described in modern literature.

2. MATHEMATICAL FORMULATION

The contact pressure in an interference fit is obtained from Lamé's equations, considering the radial deformations of the shaft and the hub [16]. This approach allows analyzing how geometry, elastic properties, and interference affect the stress distribution and, consequently, the performance of the joint. The contact pressure equation for the shaft–hub assembly is:

$$p = \frac{\delta}{\frac{d}{E_o}\left(\frac{{d_o}^2+d^2}{{d_o}^2-d^2}+v_o\right)+\frac{d}{E_i}\left(\frac{d^2+{d_i}^2}{d^2-{d_i}^2}-v_i\right)} \tag{1}$$

where d is the nominal diameter of the shaft, d_i is the internal diameter (if any) of the shaft, d_o is the external diameter of the hub, E is Young's modulus, and v is Poisson's ratio, with subscripts o and i referring to the outer element (hub) and the inner element (shaft), respectively. Meanwhile, δ represents the diametral interference between the shaft and the hub, that is, the difference between the outer diameter of the shaft and the inner diameter of the hub [16]. In the case of a solid shaft (d_i = 0), the contact pressure equation simplifies.

$$p = \frac{\delta}{\frac{d}{E_o}\left(\frac{{d_o}^2+d^2}{{d_o}^2-d^2}+v_o\right)+\frac{d}{E_i}(1-v_i)} \tag{2}$$

These Lamé equations assume that the contact surfaces are smooth; however, surface roughness modifies the effective interference and the pressure distribution at the contact interface.

2.1 Characterization of surface roughness

The turning process produces a periodic surface roughness that depends on two fundamental parameters:

- **Depth of cut:** This affects the amplitude of the roughness. The greater the depth of cut, the more pronounced the generated roughness will be.
- **Feed rate:** This influences the wavelength of the roughness. A higher feed rate increases the distance between the roughness peaks, while a lower feed rate produces a more compact surface texture.

Figure 1 shows a graphical representation of the depth of cut and feed rate parameters in relation to the type of insert and the theoretical surface roughness generated [17].

Figure 2 shows the characterization of the surface roughness in the shaft–hub joint. It is important to note that, in this model, the hub is considered smooth while the shaft presents surface roughness. On the left side (Figure 2a), a roughness profile is shown, which depends on the depth of cut measured with a profilometer using the parameter *Rz* (the peak-to-valley height of the roughness). On the right side, this corresponds to twice the amplitude A of the sinusoidal profile (Figure 2b). Similarly, the feed rate shown on the left represents the wavelength of the sinusoidal profile.

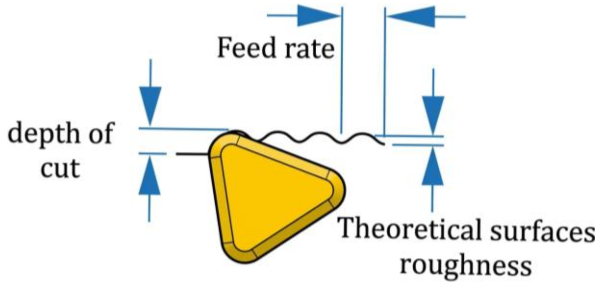

Fig. 1. Graphical representation of the depth of cut and feed rate parameters in relation to the type of insert and the theoretical surface roughness generated.

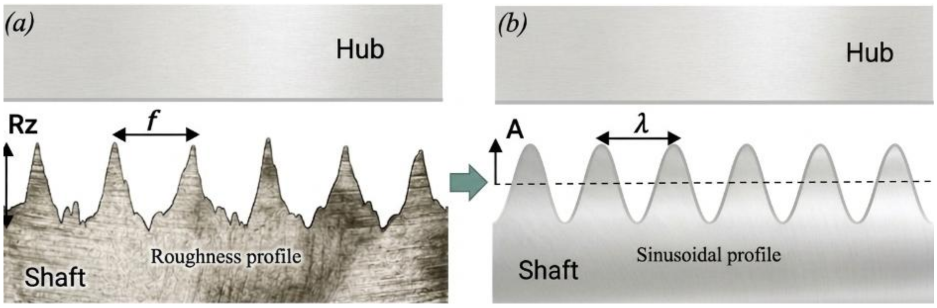

Fig. 2. Characterization of the surface roughness in the shaft–hub joint, where: (a) Roughness profile of the shaft with a smooth hub, (b) Sinusoidal profile of the shaft with a smooth hub.

2.2 Modeling of surface roughness

The periodic surface roughness generated can be mathematically modeled using a sinusoidal function, where the amplitude A is proportional to the depth of cut, and the wavelength λ is related to the feed rate of the turning process:

$$\delta_r(x) = A \cdot \sin\frac{2\pi x}{\lambda} \tag{3}$$

where:

- $\delta_r(x)$: Variation of the interference due to surface roughness.
- λ : Wavelength of the roughness, which depends on the feed rate ($\lambda \approx A_v$)
- x : Position along the contact surface.
- A : Amplitude of the roughness, related to the parameter R_z, by $A = {R_z}/{2}$
- R_z : Empirically linked to the cutting parameters (according to ISO 4287 [18]) by:

$$R_z = \frac{f^2}{8r_\varepsilon} \tag{4}$$

where f is the feed rate and r_ε is the tool nose radius. This formulation is based on previous studies that model surface roughness as a series of periodic undulations, as detailed in [19] and [20].

The tool nose radius r_ε directly influences the surface finish and the resulting roughness. Common nose radius values are:

- 0.2 – 0.4 mm: Fine finishing
- 0.4 – 0.8 mm: Semi-finishing
- 0.8 – 1.6 mm: Roughing and deeper cuts

The insert used in the experimental tests from the previous chapter was DCMT 3–55º, which is standardized according to ISO 1832 [21]. Each letter and number specifies the insert's geometry, clamping type, and dimensions.

For the DCMT 3–55º insert:

D → Rhombic shape (55º)

C → Positive clearance angle (7º)

M → Medium tolerance

T → Clamping with hole and slot

3 → Insert size

55º → Included angle

Available nose radii (r_ε): 0.2, 0.4, 0.8 mm (finishing and semi-finishing)

2.3 Total interference in the shaft–hub joint

The total interference $\delta_{\text{total}}(x)$ between the shaft and the hub is the result of the nominal interference δ_0 (designed to ensure the proper fit between both parts) and the additional interference $\delta_{\text{r}}(x)$ caused by surface roughness:

$$\delta_{total}(x) = \delta_0 + A \cdot \sin\left(\frac{2\pi}{\lambda}x\right) \tag{5}$$

This interference varies along the contact length due to the sinusoidal nature of the surface roughness, resulting in a non-uniform distribution of contact pressure between the two surfaces. This follows the approach of the variable interference theory applied to surface contact, as described by Johnson (1985) [2].

The total interference $\delta_{\text{total}}(x)$ in the shaft–hub joint depends on the positioning of the roughness profiles relative to the nominal dimension (peaks, mean line, or valleys). This positioning is directly related to the machining process and the measurement of the part. Figure 3 shows three roughness configurations with respect to the nominal diameter of the shaft.

- **Case 1. Peaks:** $\delta_{total}(x) = \delta_{01} + \delta_r(x)$ where: $\delta_{01} = \delta_0 - \frac{Rz}{2}$
- **Case 2. Mean line:** $\delta_{total}(x) = \delta_{02} + \delta_r(x)$ where: $\delta_{02} = \delta_0$
- **Case 3. Valleys:** $\delta_{total}(x) = \delta_{03} + \delta_r(x)$ where: $\delta_{03} = \delta_0 + \frac{Rz}{2}$

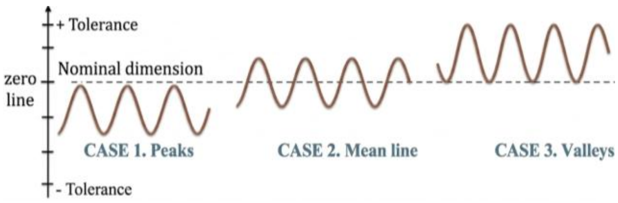

Fig. 3. Consideration of the position of roughness profiles in relation to the nominal dimension.

The first case assumes that the roughness peaks coincide with the nominal dimension; therefore, half of the *Rz* parameter is subtracted from the nominal value. This consideration is more common in machining operations performed on conventional lathes.

The second case assumes that the roughness profile is centered on the nominal dimension, maintaining the same value. This consideration is most frequently used in theoretical analyses.

The third cae assumes that the valleys of the roughness profile lie above the nominal dimension, requiring the addition of half of the *Rz* parameter. This case is more common in machining processes performed on CNC lathes.

2.4 Number of roughness peaks along the contact length

Since the roughness is periodic, the number of crests within the contact length L_c is:

$$N = \frac{L_c}{\lambda} \tag{6}$$

This parameter determines the number of roughness features, and for each roughness element, there is a variation in contact pressure and friction within the joint.

2.5 Contact pressure with a sinusoidal profile

The contact pressure $p(x)$ along the interface is obtained using Equation 7, where the total interference $\delta_{\text{total}}(x)$ is considered as the sum of the nominal interference δ_0 and the sinusoidal roughness interference $\delta_{\text{r}}(x)$.

$$p(x) = \frac{\delta_{total}(x)}{\frac{d}{E_o}\left(\frac{{d_o}^2+d^2}{{d_o}^2-d^2}+v_o\right)+\frac{d}{E_i}(1-v_i)} \tag{7}$$

2.6 Effective contact area

To determine the effective contact area, or real contact area, the following equation is used:

$$A_{real} = \pi d L_c * F_c \tag{8}$$

The contact factor F_c represents the fraction of the nominal contact area that effectively supports the load. In the present model, it is calculated from the ratio between the mean contact pressure P_m and the material hardness H, according to Eq. (9), following the real contact area approach of Bowden and Tabor [22].

$$F_c = \frac{A_{real}}{A_{geom}} = \frac{P_m}{H} \qquad (9)$$

2.7 Local friction coefficient

The friction coefficient varies locally due to changes in the amplitude and wavelength of the roughness profile. A nominal friction coefficient is used, and a correction factor is added as a function of the variation in roughness and the material properties (see equation).

$$\mu(x) = \mu_0 + k_r \cdot \sin\left(\frac{2\pi}{\lambda}x\right) \qquad (10)$$

where:

- $\boldsymbol{\mu_0}$**:** Nominal friction coefficient obtained from tables for smooth material pairs. Table 1 presents the values of μ_0 for medium-interference fits.
- $\boldsymbol{k_r}$**:** Factor that describes the influence of surface roughness on the friction coefficient and is determined through tribological tests. Table 2 shows typical k_r values according to roughness and material.

Table 1. Nominal friction coefficient μ_0 for interference fits (medium interference, dry condition) [2, 22].

Material pair	**Typical Range** μ_0	**Calculated value** μ_0
Steel – Steel	0.20 – 0.28	0.22
Steel – Bronze	0.12 – 0.18	0.15
Steel – Aluminum	0.20 – 0.30	0.25
Aluminum – Aluminum	0.35 – 0.50	0.40

Table 2. Values of the roughness influence factor k_r on the nominal friction coefficient μ_0 for different materials.

Roughness *Ra* (µm)	$\boldsymbol{k_r}$		
	Steel – Steel	Steel – Aluminum	Steel – Bronze
0.2 – 0.4	0.005 – 0.010	0.004 – 0.008	0.003 – 0.007
0.5 – 0.8	0.010 – 0.020	0.008 – 0.015	0.007 – 0.013
0.9 – 1.5	0.020 – 0.035	0.015 – 0.030	0.013 – 0.025
1.6 – 3.2	0.035 – 0.050	0.030 – 0.045	0.025 – 0.040
3.3 – 6.3	0.050 – 0.070	0.045 – 0.065	0.040 – 0.060

This equation captures the influence of surface roughness on the variation of the friction coefficient, which can affect the sliding resistance between the two contacting surfaces, following an approach similar to that presented by Bowden and Tabor [22].

2.8 Extraction force

The extraction force F_{ext} required to slide the shaft out of the hub is directly related to the contact pressure and the friction coefficient. It can be calculated by integrating the contact pressure multiplied by the friction coefficient along the contact length.

$$F_{ext} = \pi \cdot d \int_0^{L_c} p(x)\,\mu(x)\,dx \qquad (11)$$

This integral provides an estimate of the extraction force of the shaft–hub joint, considering the combined effects of interference, surface roughness, and friction. It is influenced by the depth of cut (through the amplitude A) and the feed rate (through the wavelength λ).

2.9 Calculation Procedure

To enhance the readability of the mathematical framework, Figure 4 presents a flowchart of the proposed analytical model. It details the sequential calculation steps, from defining the initial geometry and machining parameters, through the evaluation of surface topography and contact mechanics, to the final computation of the extraction force. This visual guide facilitates the implementation of the model as a computationally efficient tool.

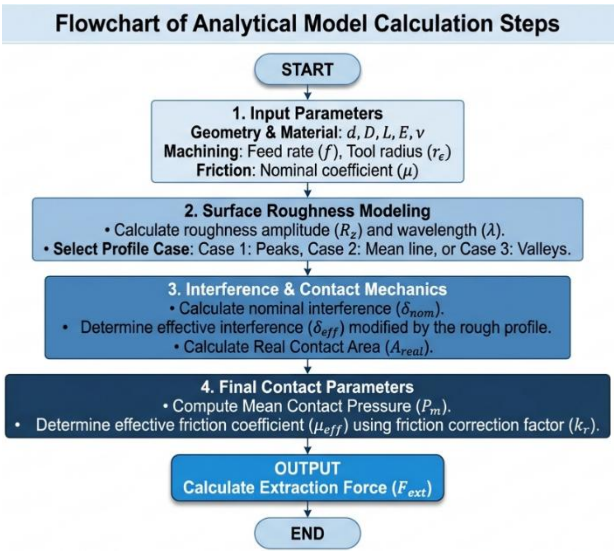

Fig. 4. Flowchart of the proposed analytical model, illustrating the calculation steps from input parameters to the final extraction force.

3. RESULTS AND DISCUSSION

3.1 Parametric study

After obtaining the mathematical model of surface roughness in relation to the shaft–hub joint, a parametric study was carried out by varying the feed rate f from 0.1 to 0.5 mm/rev to determine the roughness parameter Rz, the number of crests n within the contact length L_c, the mean pressure P_m, the real contact area A_{real}, the effective friction coefficient μ_{eff}, and the extraction force F_{ext} for each case study (peaks, mean line, and valleys). The input parameters used in the parametric study are shown in Table 3.

Table 3. Input parameters for the parametric study.

Input parameters			
d	18.880 mm	E_i	210 000 MPa
d_o	25.05 mm	E_o	210 000 MPa
δ_0	20 μm	ν_i	0.30
L_C	15 mm	ν_o	0.30
f	0.1 – 0.5 mm/rev	H	2000 MPa
μ_o	0.22	r_ε	0.40 mm

3.2 Results tables

The results obtained from the parametric study of the shaft–hub interference fit as the feed rate increases under three phase scenarios between the surfaces. Table 4 presents the results of the shaft–hub joint by varying the feed rate f for Case 1: peaks. It is observed that:

- ***Rz* vs *f***: Rz increases sharply with f.
- ***N* (crests):** decreases approximately as $N \approx L_c / f$ (for example, with $L_c \approx 15$ mm: 15/0.05 = 300, 15/0.10 = 150…), meaning fewer crests at higher feed rates, resulting in more widely spaced and taller crests.
- **P_m:** decreases monotonically from 48.045 to 10.60 MPa (−78 %). A rougher surface reduces the effective interference due to higher local deformation—contact stiffness drops and so does mean pressure.
- **A_{real}:** also decreases in the same proportion as P_m (−78 %, from 21.37 to 4.72 mm^2), indicating increasingly partial contact (patches at crests) rather than continuous contact.
- **μ_{eff}:** increases slightly (0.22 to 0.27). Higher roughness promotes plowing/interlocking components that raise friction.
- **F_{ext}:** despite the slight increase in μ, it drops significantly from 9404 N to 2582 N (−72.5 %). The dominant effect is the loss of P_m and **A_{real}**: the μ increment is insufficient to compensate.

Table 5 presents the results of the shaft–hub joint by varying the feed rate f for Case 2: mid-shaft. It is observed that:

- **P_m:** Remains practically constant in the range f = 0 – 0.30 (around 48 MPa) and then increases slightly from f = 0.35 to 0.50 (by about 20%).
- **A_{real}:** Maintains a value of 21.37 mm^2 up to f = 0.30 and then rises to 25.75 mm^2 at f = 0.50 (an increase of 20%). More loaded asperities flatten/interlock, increasing the bearing area.
- **μ_{eff}:** Increases from 0.220 to 0.259 (18%).
- **F_{ext}:** Rises from 9404 N (smooth surface) to 13,364 N at f = 0.50 (a 42% increase).

Table 6 presents the results of the shaft–hub joint by varying the feed rate f for Case 3: valleys. It is observed that:

- **P_m:** Increases sharply and convexly from 48 to 142 MPa (+196%).
- **A_{real}:** Also rises significantly from 21.37 to 63.12 mm^2 (+195%).
- **μ_{eff}:** Increases slightly from 0.220 to 0.240 (+9%).
- **F_{ext}:** Shoots up from 9404 N (smooth surface) to 30,276 N at f = 0.50 (+222%).

Table 4. Results of the shaft–hub joint by varying the feed rate *f* for Case 1 (peaks).

f (mm/rev)	Rz (μm)	N (crests)	P_m (MPa)	A_{real} (mm^2)	μ_{eff}	F_{ext} (N)	% smooth
0	0	0	48.045	21.3728	0.2200	9404.03	0.00
0.05	0.78	300	47.1066	20.9553	0.2201	9223.48	-1.92
0.10	3.12	150	44.2915	19.7030	0.2206	8694.38	-7.55
0.15	7.03	100	39.5996	17.6158	0.2245	7910.64	-15.88
0.20	12.5	75	33.0309	14.6938	0.2297	6749.12	-28.23
0.25	19.53	60	24.5855	10.9368	0.2486	5438.37	-42.17
0.30	28.12	50	18.8560	8.3880	0.2609	4376.98	-53.46
0.35	38.28	42.86	15.7277	6.9964	0.2665	3730.74	-60.33
0.40	50	37.5	13.6672	6.0798	0.2699	3283.21	-65.09
0.45	63.28	33.33	12.0433	5.3574	0.2721	2915.21	-69.00
0.50	78.12	30	10.6006	4.7156	0.2737	2582.23	-72.54

Table 5. Results of the shaft–hub joint by varying the feed rate *f* for Case 2 (mid-shaft).

f (mm/rev)	Rz (μm)	N (crests)	P_m (MPa)	A_{real} (mm^2)	μ_{eff}	F_{ext} (N)	% smooth
0	0	0	48.045	21.3728	0.22	9404.03	0.00
0.05	0.78	300	48.045	21.3728	0.2201	9407.16	0.03
0.10	3.12	150	48.045	21.3728	0.2206	9429.07	0.27
0.15	7.03	100	48.045	21.3728	0.2237	9563.70	1.70
0.20	12.5	75	48.045	21.3728	0.2266	9687.88	3.02
0.25	19.53	60	48.045	21.3728	0.2346	10030.19	6.66
0.30	28.12	50	48.045	21.3728	0.2411	10305.70	9.59
0.35	38.28	42.86	48.10018	21.3973	0.2488	10649.65	13.25
0.40	50	37.5	50.16032	22.3138	0.2546	11360.66	20.81
0.45	63.28	33.33	53.7404	23.9064	0.2576	12313.79	30.94
0.50	78.12	30	57.89533	25.7547	0.2594	13364.51	42.11

Table 6. Results of the shaft–hub joint by varying the feed rate *f* for Case 3 (valleys).

f (mm/rev)	Rz (μm)	N (crests)	P_m (MPa)	A_{real} (mm^2)	μ_{eff}	F_{ext} (N)	% smooth
0	0	0	48.045	21.3728	0.22	9404.03	0.00
0.05	0.78	300	48.9834	21.7902	0.2201	9590.83	1.99
0.10	3.12	150	51.7985	23.0425	0.2205	10163.77	8.08
0.15	7.03	100	56.4904	25.1297	0.2232	11216.75	19.28
0.20	12.5	75	63.0591	28.0518	0.2251	12626.65	34.27
0.25	19.53	60	71.5045	31.8087	0.2298	14622.00	55.49
0.30	28.12	50	81.8266	36.4005	0.2324	16917.90	79.90
0.35	38.28	42.86	94.0807	41.8518	0.2348	19653.03	108.99
0.40	50	37.5	108.6102	48.3152	0.2371	22910.62	143.63
0.45	63.28	33.33	124.6138	55.4344	0.2388	26468.26	181.46
0.50	78.12	30	141.8829	63.1165	0.2398	30275.90	221.95

3.3 Roughness Rz vs. Feed rate

Figure 5 shows the graph of the roughness parameter R_z as a function of feed rate (f = 0–0.5 mm/rev). The curve exhibits a convex, increasing trend: as f increases, R_z rises progressively faster.

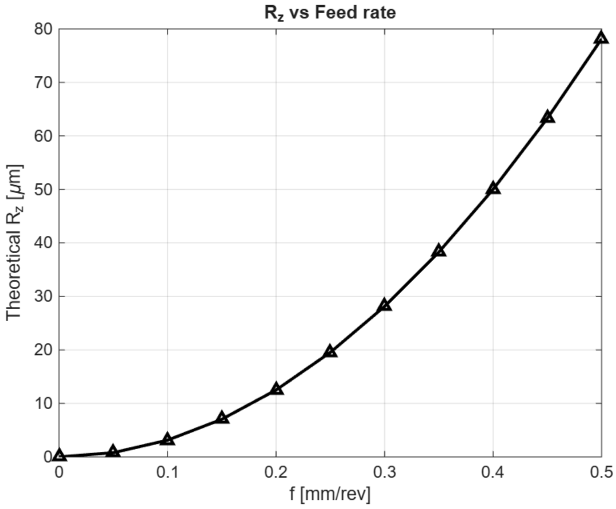

Fig. 5. Graph of the roughness parameter *Rz* as a function of feed rate (f = 0–0.5 mm/rev).

3.4 Number of crests vs. Feed rate

Figure 6 illustrates a rapid hyperbolic decrease in the number of crests (N) along L_c as feed rate (f) increases.

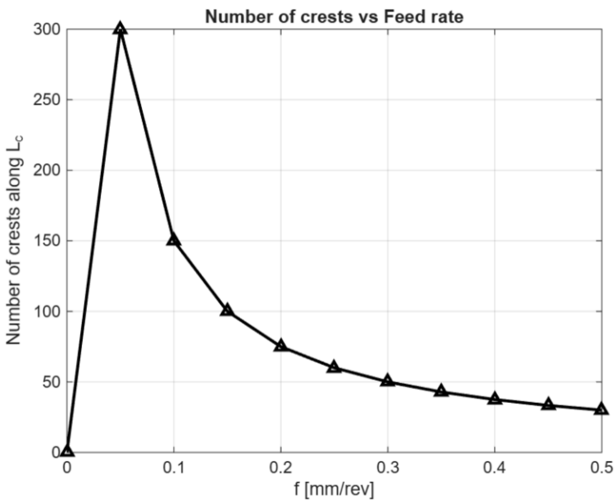

Fig. 6. Graph of the number of crests N along the contact length L_c as the feed rate f increases during turning.

With fewer crests (small N) and higher R_z (typical of high f), the dispersion among the cases increases, as confirmed by the results tables:

- **Case 1 – Peaks:** Mean pressure and real contact area decrease, leading to a reduction in extraction force.
- **Case 2 – Mean line:** Mean pressure remains stable, while real contact area and extraction force increase moderately.
- **Case 3 – Valleys:** Additional interference occurs, causing a sharp rise in mean pressure, real contact area, and extraction force.

3.5 Roughness profiles

Five sinusoidal profiles were plotted for f = 0.10, 0.20, 0.30, 0.40, and 0.50 mm/rev over L_c = 15 mm, where the wavelength $\lambda \approx f$ and the wave amplitude $A \approx R_z/2$. It is observed that as f increases, the waves become taller and more widely spaced (Figure 7).

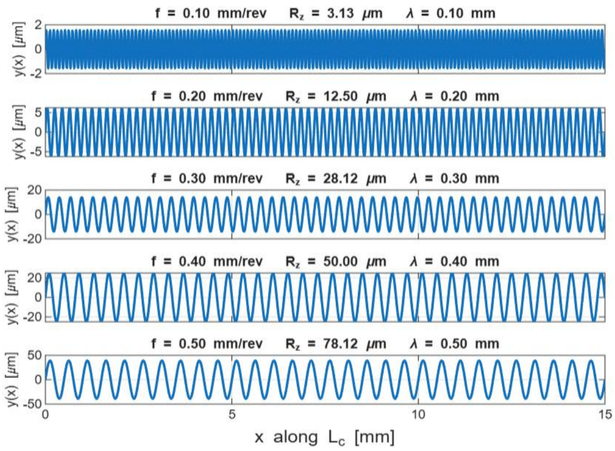

Fig. 7. Roughness profiles for each feed rate along the contact length.

3.6 Contact pressure

Figure 8 shows the variation of mean pressure as a function of feed rate for each case (peaks, mid-shaft, valleys), where the following trends are observed:

- **Case 1 – Peaks (blue):** starts at 48 MPa and decreases almost monotonically to 10.60 MPa at f = 0.5 mm/rev.
- **Case 2 – Mean line (red):** remains nearly flat at 48 MPa up to f = 0.35 and then rises slightly to 57.89 MPa at f = 0.5 mm/rev.
- **Case 3 – Valleys (green):** shows a convex growth from 48 MPa to 141.88 MPa between f = 0 and 0.5 mm/rev (a large increase).

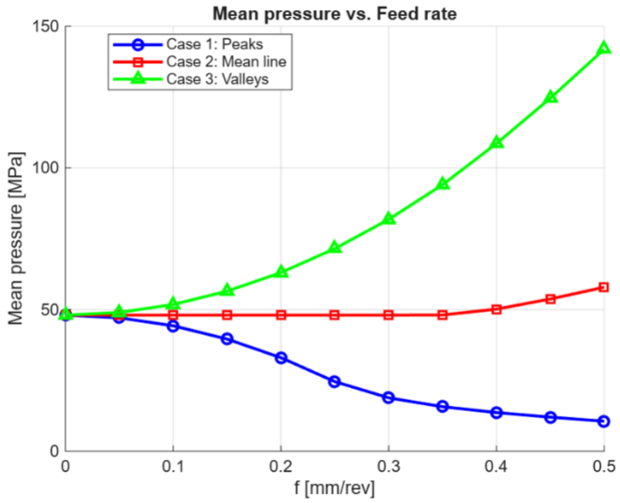

Fig. 8. Graph of the variation of mean pressure with feed rate for each case (peaks, mid-shaft, valleys).

Local pressure profiles $p(x)$ were also obtained along the contact length L_c (Figure 9) for different feed rates f in each case (peaks, mean line, valleys). The pressure is periodic, and its wavelength coincides with the surface roughness ($\lambda \approx f$), while the amplitude of the oscillations increases with R_z. In particular, the following behavior is observed:

- **Peaks (blue):** the baseline decreases with *f*, and the valleys approach very low-pressure values.
- **Mean line (red):** remains almost constant up to f = 0.30, after which the contact pressure increases slightly.
- **Valleys (green):** the baseline rises sharply, and at high *f* values, very high-pressure peaks appear.

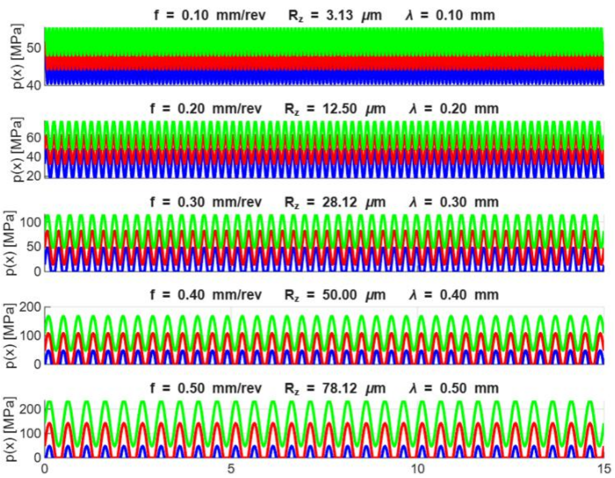

Fig. 9. Contact pressure profiles $p(x)$ for each feed rate along the contact length.

3.7 Effective contact area vs. Feed rate

Figure 10 shows how the effective contact area $A_{effective}$ changes with feed rate f for each case (peaks, mean line, valleys), where:

- **Case 1 – Peaks (blue):** A_{real} decreases from 21.37 to 4.72 mm^2 as *f* increases from 0 to 0.5 mm/rev (−78%).
- **Case 2 – Mid-shaft (red):** A_{real} remains constant at 21.37 mm^2 up to f = 0.30 and then increases slightly to 25.75 mm^2 at f = 0.50 (+20%).
- **Case 3 – Valleys (green):** increases convexly from 21.37 to 63.12 mm^2 (+195%).

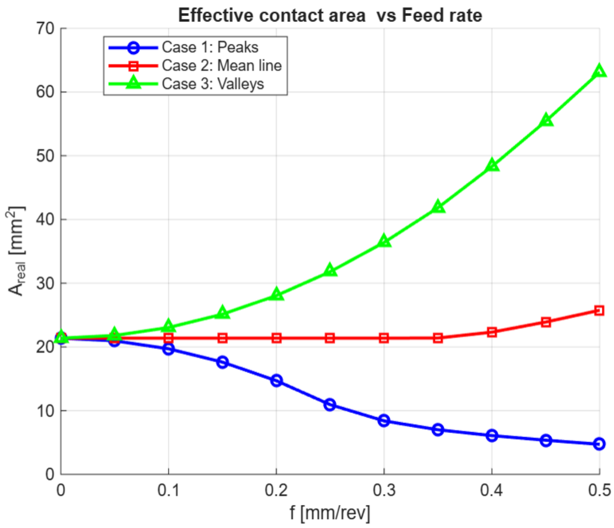

Fig. 10. Graph of the variation of effective contact area (A_{real}) with feed rate (*f*) for each case (peaks, mean line, valleys).

3.8 Friction coefficient

Figure 11 summarizes how the effective friction coefficient *μ_eff* changes with feed rate *f* for the three surface phase cases, showing that:

- **Case 1 – Peaks (blue):** *μ_eff* increases from 0.220 to 0.273 (Δ ≈ +0.053). The rise becomes steeper from f = 0.22–0.25.
- **Case 2 – Mean line (red):** increases from 0.220 to 0.259 (Δ ≈ +0.039), showing an almost linear growth from f = 0.25.
- **Case 3 – Valleys (green):** increases from 0.220 to 0.240 (Δ ≈ +0.020), the smallest and smoothest increment.

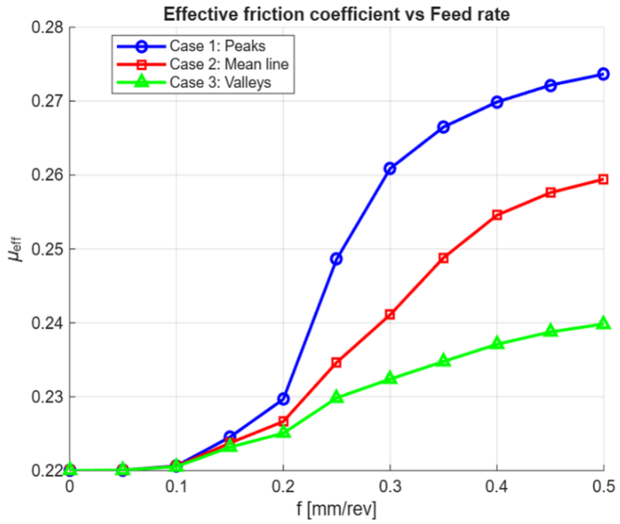

Fig. 11. Graph of the variation of the effective friction coefficient (μ_{eff}) with feed rate (f) for the three surface roughness phases

Figure 12 shows the local profiles of the friction coefficient $\mu(x)$ along the contact length L_c for different feed rates f (with the corresponding Rz and wavelength λ values indicated). Two main characteristics can be observed:

- **Periodicity:** $\mu(x)$ is periodic, and its wavelength $\lambda \approx f$. As f increases, the waves become more widely spaced (fewer crests along Lc).
- **Amplitude:** The local variation of μ increases with R_z (and thus with f). At f = 0.10, the profile is nearly uniform, while at f = 0.50 pronounced oscillations appear. Furthermore, the effective friction coefficient μ_{eff} increases with feed rate f.

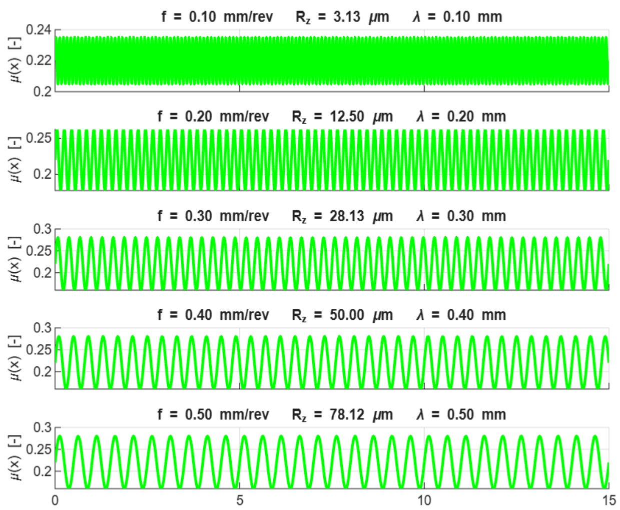

Fig. 12. Variation of the friction coefficient $\mu(x)$ for each feed rate

3.9 Extraction force

Figure 13 summarizes the extraction force F_{ext} as a function of the feed rate f for the three roughness consideration cases (peaks, mean line, valleys), where:

- **Case 1 – Peaks (blue):** F_{ext} decreases from 9.4 kN (smooth) to 2.6 kN at f = 0.50 (−72%). The drop is almost monotonic and becomes steeper beyond f = 0.20.
- **Case 2 – Mean line (red):** F_{ext} increases slightly from 9.4 kN (smooth) to 13.4 kN at f = 0.50 (+42%), showing a slightly convex curve from f = 0.30.
- **Case 3 – Valleys (green):** exhibits a pronounced convex growth from 9.4 kN to 30.3 kN (+222%). At f = 0.35, it already exceeds twice the smooth-surface value.

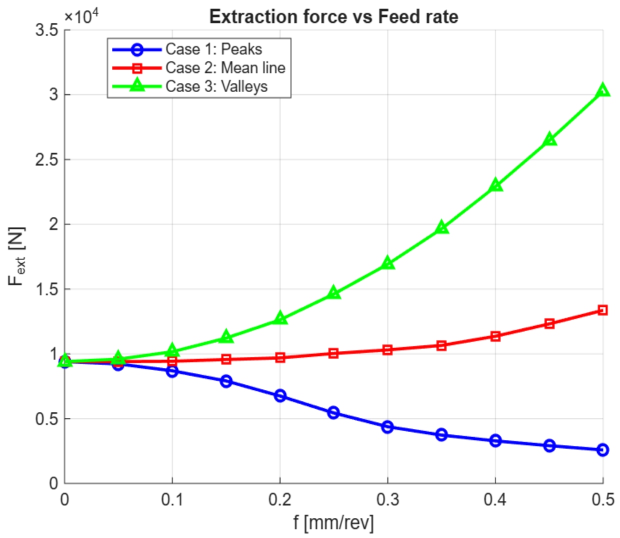

Fig. 13. Graph of the extraction force F_{ext} as a function of feed rate f for the three roughness consideration cases.

3.10 Discussion

The parametric study demonstrates that increasing the feed rate significantly alters the contact mechanics within the interference fit, producing distinct behaviors depending on the surface phase (peaks, mean line, or valleys).

For Case 1 (Peaks), both mean pressure and effective contact area decreased notably (−78%), resulting in a sharp drop in extraction force (−72%). This trend aligns with the elastic–plastic contact analyses by Kogut and Etsion [23], who reported that reduced real contact area due to asperity-dominated contact lowers load capacity. These results also coincide with the finite-element simulations of Salgado-Cruz et al. [6], which showed that rougher surfaces weaken press-fit resistance due to diminished contact stiffness.

In Case 2 (Mean line), pressure remained stable while area and friction coefficient increased slightly, producing a moderate 42% rise in extraction force. This correlates with the observations of Woo and Thomas [20], who identified an optimal surface roughness where adhesion and plowing effects are balanced. Additionally, Salgado-Cruz et al. [7] found experimentally that moderate feed rates in CNC turning increased the assembly/disassembly force, behavior analogous to our mean-line case.

For Case 3 (Valleys), pressure and real contact area rose dramatically (+195%), leading to a 222% increase in extraction force. Similar effects were described by Bowden and Tabor [22], who showed that valley-dominated topographies sustain higher pressures and frictional interlocking. The results are also consistent with those reported by Salgado-Cruz et al. [7], who observed increased resistance in joints machined with higher feed rates that generate valley-type profiles.

Overall, the developed mathematical model successfully captures the combined geometric and tribological effects of surface roughness on interference-fit performance, reproducing trends found experimentally [6,7] and in classical tribological theory [1–3]. This analytical approach thus bridges machining parameters and mechanical behavior, providing a predictive tool for design and optimization of press-fit assemblies.

3.11 Influence of surface profile assumptions on contact parameters

As summarized in Table 7, the valley dominated surface profile exhibits a drastic increase in extraction force (F_{ext}) compared to the smooth and peak dominated cases. When the roughness valleys are geometrically distributed above the nominal dimension, the effective interference increases significantly. The rigid asperities of the shaft penetrate deeper into the hub material, generating severe local elastic deformation. This micro-topographical indentation creates a mechanical 'interlocking' effect between the mating surfaces. Consequently, the real contact area (A_{real}) and the mean contact pressure (P_{m}) expand by nearly 195%, acting as a robust physical barrier against axial sliding and ultimately raising the joint's extraction capacity by up to 222%.

Table 7. Percentage variations of contact parameters at maximum feed rate (f = 0.50 mm/rev) compared to a smooth surface.

Surface Profile Case	Δ P_{m} (%)	Δ A_{real} (%)	Δ μ_{eff} (%)	Δ F_{ext} (%)
Case 1 (Peaks)	- 78.0	- 78.0	24.1	- 72.5
Case 2 (Mean line)	20.5	20.5	17.9	42.1
Case 3 (Valleys)	195.3	195.3	9.0	221.9

3.12 Validation of the Analytical Model

To verify the accuracy and reliability of the proposed mathematical model, the analytically predicted extraction forces (F_{ext}) were compared against previously published experimental and numerical data by Salgado-Cruz et al. [7]. In those previous studies, shaft-hub assemblies were manufactured using CNC turning under controlled feed rates (f), and the required setting/extraction efforts were evaluated both experimentally and via Finite Element Analysis (FEA).

Figure 14 shows the overlay plot comparing the analytical extraction forces derived from our current theoretical model with the experimental data points extracted from the literature [7]. As observed, the classical smooth-surface assumption (f = 0) significantly underestimates the actual mechanical strength of the joint. However, as the feed rate increases, the experimental data aligns closely with the analytical predictions of the roughness-modified models.

Specifically, the experimental trend falls within the boundaries established by the "Valleys" profile assumptions. This demonstrates that the physical phenomenon of micro topographical interlocking which significantly increases the real contact area and contact pressure is accurately captured by the proposed mathematical formulation. The slight deviations at higher feed rates can be attributed to localized plastic deformations of the asperities, an effect that is partially idealized in this purely elastic mathematical model, but overall, the correlation validates the analytical approach for engineering design purposes.

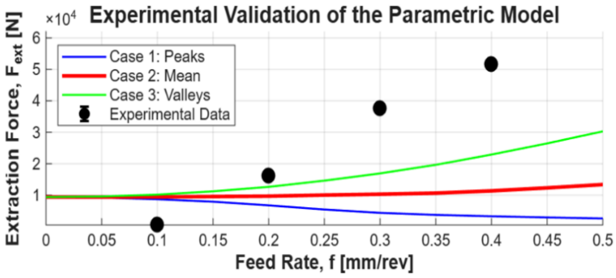

Fig. 14. Overlay plot of extraction force (F_{ext}) versus feed rate (*f*), comparing the proposed mathematical models for different surface profile assumptions (Peaks, Mean line, Valleys) with experimental measurements [7].

4. CONCLUSIONS

The developed analytical model successfully incorporates surface roughness effects into the mechanical behavior of shaft–hub interference fits. By coupling turning parameters with contact mechanics, the model predicts the influence of amplitude and wavelength on contact pressure, real contact area, friction coefficient, and extraction force. The results demonstrate that surface topography has a decisive impact on joint performance: peak-dominated profiles reduce load capacity, while valley-dominated profiles enhance pressure transmission and extraction strength.

The proposed formulation provides a rapid and reliable analytical alternative to finite element simulations, reducing computational effort while preserving physical accuracy. Furthermore, it establishes a direct link between machining parameters and mechanical functionality, offering a practical tool for optimizing feed rate and surface finish to improve reliability, torque capacity, and tribological efficiency of interference-fit assemblies. Future work may extend the model to include thermal effects and material plasticity for a more comprehensive analysis.

REFERENCES

[1] J. R. Barber, *Contact Mechanics*, 1st ed. Cham, Switzerland: Springer Nature, 2018. doi: 10.1007/978-3-319-70939-0.

[2] K. L. Johnson, *Contact Mechanics*. Cambridge, UK: Cambridge University Press, 1985. doi: 10.1017/CBO9781139171731.

[3] J. A. Williams, *Engineering Tribology*. Cambridge, UK: Cambridge University Press, 2005. doi: 10.1017/CBO9780511805905.

[4] E. Izard, R. García-Martín, M. Rodríguez-Martín, and M. Lorenzo, "Influence of the friction coefficient on the stress distributions and contact pressure in press-fits via finite element analysis," *Lubricants*, vol. 11, no. 11, p. 472, Nov. 2023, doi: 10.3390/lubricants11110472.

[5] H. L. Au-Yeung, S. Ataya, H. Hassanin, M. A. El-Sayed, M. Ahmadein, N. A. Alsaleh, M. M. Z. Ahmed, and K. Essa, "Non-destructive disassembly of interference fit under wear conditions for sustainable remanufacturing," *Machines*, vol. 11, no. 5, p. 538, May 2023, doi: 10.3390/machines11050538.

[6] M. Salgado-Cruz, C. Cortés-García, D. Szwedowicz, and E. Martínez-Rayón, "Strength of the shaft/hub joint using a finite element model," *Journal of Scientific and Technical Applications*, vol. 5, no. 15, pp. 9-18, Dec. 2019, doi: 10.35429/JSTA.2019.15.5.9.18.

[7] M. Salgado-Cruz, C. Cortés-García, D. Szwedowicz, E. Martínez-Rayón, Q. Estrada-Barbosa, and A. Blanco-Ortega, "Required effort for shaft/ring setting according to roughness due to CNC lathe machining," *DYNA*, vol. 96, no. 1, pp. 85-90, Jan. 2021, doi: 10.6036/9727.

[8] W. H. Yang and Y. S. Tarng, "Design optimization of cutting parameters for turning operations based on the Taguchi method," *Journal of Materials Processing Technology*, vol. 84, no. 1-3, pp. 122-129, Nov. 1998, doi: 10.1016/S0924-0136(98)00079-X.

[9] D. Stamenkovic, M. Milosevic, M. Mijajlović, and M. S. Banic, "Estimation of the static friction coefficient for press fit joints," *Journal of the Balkan Tribological Association*, vol. 17, no. 3, pp. 341-355, Sep. 2011.

[10] J. Abdo and K. Farhang, "Elastic-plastic contact model for rough surfaces based on plastic asperity concept," *International Journal of Non-Linear Mechanics*, vol. 40, no. 4, pp. 495-506, May 2005, doi: 10.1016/j.ijnonlinmec.2004.08.003.

[11] L. Esposito, M. Bruno, and A. Bertocco, "Analytical formulation of the contact pressure evolution for interference joints under creep regime," *International Journal of Pressure Vessels and Piping*, vol. 185, p. 104126, 2020, doi: 10.1016/j.ijpvp.2020.104126.

[12] R. L. Jackson and J. L. Streator, "A multi-scale model for contact between rough surfaces," *Wear*, vol. 261, no. 11/12, pp. 1337-1347, Dec. 2006, doi: 10.1016/j.wear.2006.03.015.

[13] J. A. Greenwood and J. B. P. Williamson, "Contact of nominally flat surfaces," *Proceedings of the Royal Society of London a Mathematical and Physical Sciences*, vol. 295, no. 1442, pp. 300-319, 1966, doi: 10.1098/rspa.1966.0242.

[14] B. Li, P. Li, R. Zhou, X. Feng, and K. Zhou, "Contact mechanics in tribological and contact damage-related problems: A review," *Tribology International*, vol. 171, p. 107534, Mar. 2022, doi: 10.1016/j.triboint.2022.107534.

[15] C. Breuning, M. Plogmeyer, C. Pongratz, M. Wagner, A. Schott, M. Kreimeyer, and G. Bräuer, "Influence of thin-film coatings on the joining process of shaft-hub connections," *Machines*, vol. 13, no. 9, p. 776, Sep. 2025, doi: 10.3390/machines13090776.

[16] R. G. Budynas and J. K. Nisbett, Shigley's Mechanical Engineering Design, 8th ed. New York, NY, USA: McGraw-Hill, 2008.

[17] ASM International Handbook Committee, ASM Handbook, Volume 16: *Machining*. Materials Park, OH, USA: ASM International, 1989. doi: 10.31399/asm.hb.v16.9781627081887.

[18] Geometrical Product Specifications (GPS)—Surface texture: Profile method—Terms, definitions and surface texture parameters, ISO Standard 4287:1997, 1997.

[19] M. Storchak and M. A. Lekveishvili, "Improvement of analytical model for oblique cutting-Part I: Identification of mechanical characteristics of machined material," *Metals*, vol. 13, no. 10, p. 1750, Oct. 2023, doi: 10.3390/met13101750.

[20] K. L. Woo and T. R. Thomas, "Contact of rough surfaces: A review of experimental work," *Wear*, vol. 58, no. 2, pp. 331-340, Feb. 1980, doi: 10.1016/0043-1648(80)90162-3.

[21] Indexable inserts for cutting tools—Designation, ISO Standard 1832:2017, 2017.

[22] F. P. Bowden and D. Tabor, The Friction and Lubrication of Solids. Oxford, UK: Oxford Univ. Press, 1950.

[23] L. Kogut and I. Etsion, "Elastic-plastic contact analysis of a sphere and a rigid flat," *Journal of Applied Mechanics*, vol. 69, no. 5, pp. 657-662, Sep. 2002, doi: 10.1115/1.1490373.